

1 **The Airborne Cloud-Aerosol Transport System, Part I: Overview and Description**
2 **of the Instrument and Retrieval Algorithms**

3 John E. Yorks^{1,3}, Matthew J. McGill², V. Stanley Scott², Andrew Kupchok³, Shane
4 Wake², Dennis Hlavka¹, William Hart¹, Patrick Selmer¹

5
6 ¹Science Systems and Applications, Inc. and NASA GSFC

7 ²NASA GSFC

8 ³University of Maryland - College Park

9

10 **Abstract**

11 The Airborne Cloud-Aerosol Transport System (ACATS) is a multi-channel Doppler
12 lidar system recently developed at NASA Goddard Space Flight Center (GSFC). A
13 unique aspect of the multi-channel Doppler lidar concept such as ACATS is that it is also,
14 by its very nature, a high spectral resolution lidar (HSRL). Both the particulate and
15 molecular scattered signal can be directly and unambiguously measured, allowing for
16 direct retrievals of particulate extinction. ACATS is therefore capable of simultaneously
17 resolving the backscatter/extinction properties and motion of a particle from a high
18 altitude aircraft. ACATS has flown on the NASA ER-2 during test flights over California
19 in June 2012 and science flights during the Wallops Airborne Vegetation Experiment
20 (WAVE) in September 2012. This paper provides an overview of the ACATS method
21 and instrument design, describes the ACATS retrieval algorithms for cloud and aerosol
22 properties, and demonstrates the data products that will be derived from the ACATS data
23 using initial results from the WAVE project. The HSRL retrieval algorithms developed
24 for ACATS have direct application to future spaceborne missions such as the Cloud-
25 Aerosol Transport System (CATS) to be installed on the International Space Station
26 (ISS). Furthermore, the direct extinction and particle wind velocity retrieved from the

27 ACATS data can be used for science applications such as dust or smoke transport and
28 convective outflow in anvil cirrus clouds.

29 ***1.0 Introduction***

30 Current uncertainties in the role of aerosols and clouds limit our ability to accurately
31 model the Earth's climate system and to predict climate change. There are several
32 different types of lidar systems that can be used to measure cloud and aerosol properties
33 and motion. Cloud-aerosol lidars measure the elastic backscatter from molecules and
34 atmospheric particulates to resolve vertical profiles of spatial and optical properties of
35 clouds and aerosols. The two most common elastic backscatter lidar techniques are
36 standard backscatter lidars and high spectral resolution lidars (HSRL). The data provided
37 by these lidar systems are essential to investigations of cloud and aerosol properties for
38 numerous reasons. The vertical structure of cloud and aerosol layers resolved by lidar
39 systems cannot be accurately obtained from passive satellite or passive airborne sensors.
40 Furthermore, thin cloud optical depths are often below the detection limits of millimeter
41 cloud radar systems (Comstock *et al.* 2002). In situ instruments can provide critical
42 measurements of cloud and aerosol microphysical properties. However, they do not
43 easily provide vertical profiles of these measurements and can alter the physical
44 properties of the particles (Jensen *et al.* 2009; Zhao *et al.* 2011). Information obtained
45 from cloud-aerosol lidar systems can improve knowledge of cloud and aerosol properties,
46 which in turn advance parameterizations and reduce the uncertainties introduced in
47 GCMs.

48 Standard elastic backscatter lidars are the least complex and most common lidar
49 systems used to study vertical profiles of cloud and aerosol properties. Ground-based and

50 airborne systems have been used in numerous field campaigns over the past few decades.
51 In the last decade, as laser transmitters have become more reliable, the first space-based
52 elastic backscatter lidar systems were designed and launched. The Geoscience Laser
53 Altimeter System (GLAS; Spinhirne *et al.* 2005) was launched in January 2003 and the
54 Cloud-Aerosol Lidar Infrared Pathfinder Satellite Observations project (CALIPSO;
55 Winker *et al.* 2009) was launched in April 2006. These lidar systems fundamentally
56 measure vertical profiles of attenuated total backscatter, without separation of particulate
57 (Mie) and molecular (Rayleigh) scattering. There have been many methods developed to
58 retrieve the particulate extinction and particulate backscatter coefficients from a cloud-
59 aerosol lidar return signal. One technique is an inversion using standard backscatter lidar
60 data developed by Fernald *et al.* (1972) and Klett (1981; 1985). The Klett or Fernald
61 method makes it possible to solve the standard lidar equation by assuming a ratio of
62 aerosol extinction to aerosol backscatter coefficients, referred to as the lidar ratio, is
63 known and constant throughout a particulate layer. This assumption reduces the number
64 of unknowns in the system to one. This method is commonly used to retrieve particulate
65 extinction and backscatter coefficients from standard backscatter lidars such as CALIPSO
66 (Young and Vaughan 2009) and the Cloud Physics Lidar (McGill *et al.* 2002). The lidar
67 ratio (units of sr) is highly dependent on the optical and microphysical properties of
68 atmospheric layer being measured. The lidar ratio typically varies from about 10 to 50 sr
69 for tropospheric clouds (Del Guasta *et al.* 2001; Seifert *et al.* 2007; Yorks *et al.* 2011a)
70 and from about 20 to 80 sr for aerosol particles (Ackermann 1998). For cloud and
71 aerosol layers with an optical depth greater than 0.30, a 30 percent error in the assumed

72 lidar ratio can lead to an error in the extinction retrieval from elastic backscatter lidar
73 systems greater than 50 percent (Young *et al.* 2014).

74 Another method for retrieving the particulate backscatter and extinction coefficients
75 from a lidar signal is a HSRL, which is based on the use of two measured profiles instead
76 of only one. The HSRL technique utilizes the difference in spectral distribution of the
77 molecular and particulate backscattered signals (Fiocco *et al.* 1971; Shipley *et al.* 1983;
78 Grund *et al.* 1991). High spectral resolution optical filters are required to separate the
79 particulate contribution from the molecular backscatter and resolve particulate extinction
80 and backscatter coefficients independently with no assumption about the lidar ratio
81 required. Only a few HSRL instruments have been successfully developed and operated
82 to measure cloud and aerosol optical properties from ground or aircraft platforms. The
83 iodine filter method (Piiroinen and Eloranta 1994) is the preferred method for HSRL
84 systems to date. Recently airborne HSRL systems that employ iodine filters have been
85 implemented and demonstrated on the NASA King Air (B-200) research aircraft (Hair *et*
86 *al.* 2008) and the German Aerospace Center (DLR) Falcon research aircraft (Esselborn *et*
87 *al.* 2008). However, a caveat of the iodine filter technique is that the actual particulate
88 backscatter spectral broadening is not measured but inferred from the total and molecular
89 backscatter. The backscattered signal also contains additional information that is
90 imparted in the scattering process, such as the Doppler shift caused by the mean velocity
91 of the particulate.

92 Doppler wind lidars use the frequency shift imparted on atmospheric aerosols and
93 molecules to determine vertical profiles of the horizontal wind speed and direction.
94 Providing these measurements on a global scale can progress understanding of

95 atmospheric dynamics and improve numerical weather predictions (Baker *et al.* 1995).
96 The two most common types of pulsed Doppler wind lidar systems are coherent
97 (heterodyne) detection and direct (incoherent) detection. Coherent Doppler lidars use a
98 heterodyning technique that mixes a pulsed lidar signal with a second laser signal to
99 produce a beat frequency that is related to the Doppler shift. The second continuous laser
100 beam is usually a local oscillator offset in frequency (Hall *et al.* 1984; Huffaker *et al.*
101 1984). Direct-detection lidars directly measure the frequency shift of the return signal
102 using a high spectral resolution filter, such as a Fabry-Perot interferometer or etalon, and
103 operate at shorter wavelengths than coherent systems (Benedetti-Michelangeli *et al.*
104 1972; Chanin *et al.* 1989; Garnier and Chanin 1992; Gentry and Korb 1994). One direct-
105 detection method, termed multichannel (MC) by McGill and Spinhirne (1998), measures
106 the Doppler shift by imaging the etalon fringe pattern onto a multiple element detector
107 (Abreu *et al.* 1992; Fischer *et al.* 1995) The MC direct-detection concept requires the
108 etalon transmission function to be aligned with the laser wavelength. This method was
109 demonstrated by McGill *et al.* 1997a for a ground-based lidar developed at the University
110 of Michigan.

111 A MC direct-detection Doppler lidar system capable of resolving the Doppler shifts
112 inherent to atmospheric motions can simultaneously provide information about both the
113 scattering intensity and the motion of the particle. Such an instrument was recently
114 developed at NASA Goddard Space Flight Center (GSFC) called the Airborne Cloud-
115 Aerosol Transport System (ACATS). ACATS is the first lidar system to simultaneously
116 measure cloud/aerosol properties and wind from an airborne platform. The instrument
117 has flown on the NASA ER-2 during test flights over California in June 2012 and as part

118 of the Wallops Airborne Vegetation Experiment (WAVE) in September 2012. A
119 description of the ACATS instrument design is provided, which includes details of the
120 optical and mechanical components of the subsystems as well as the software that
121 autonomously controls the instrument operation. This work advances the effort of McGill
122 *et al.* 1997a and McGill *et al.* 1997b by demonstrating the retrieval algorithms for HSRL
123 direct measurements of cloud and aerosol optical properties (i.e. extinction) that can be
124 applied to future space-based HSRL missions. This study also presents initial ACATS
125 HSRL results and data products from the WAVE campaign.

126 **2.0 ACATS Method and Instrument Description**

127 **2.1 ACATS Methodology**

128 The ACATS instrument is a multi-channel (MC) Doppler lidar system built for use on
129 the NASA ER-2 high altitude aircraft. The MC technique passes the returned
130 atmospheric backscatter through a single etalon and divides the transmitted signal into
131 several channels (wavelength intervals), which are measured simultaneously and
132 independently (Figure 1). The resulting aerosol spectral distribution is then compared to
133 the outgoing laser distribution to infer the Doppler shift, as demonstrated in Figure 2a.
134 Subsequent measurements of the atmospheric scattered light will reveal a wavelength
135 offset that is proportional to the Doppler shift and directly related to the velocity of the
136 scattering particles (Figure 2b). The basic concept is summarized in Figures 1 and 2.
137 The MC method was demonstrated using the ground-based University of Michigan
138 Doppler lidar (McGill *et al.* 1997a; McGill *et al.* 1997b).

139 A unique aspect of the MC Doppler lidar concept such as ACATS is that it is also a
140 HSRL. Both the particulate and molecular scattered signal can be directly and

141 unambiguously measured since the broad Rayleigh-scattered spectrum is imaged as a
142 nearly flat background, illustrated in Figure 2c. The integral of the aerosol-scattered
143 spectrum is analogous to the aerosol measurement from the typical absorption filter
144 HSRL technique, providing exactly the same pieces of information as a standard HSRL
145 (Figure 2d). While previous ground-based MC systems have been built and operated
146 (Benedetti-Michelangeli *et al.* 1972; Abreau *et al.* 1992; McGill *et al.* 1997a), there has
147 been no airborne demonstration of the technique and the method has not been used to
148 derive HSRL cloud and aerosol properties.

149 **2.2 ACATS Instrument Description**

150 The ACATS instrument is composed of three main subsystems; laser transmitter,
151 telescope, and receiver optics. A picture of the ACATS instrument fully assembled, with
152 the receiver and telescope subsystems, is shown in Figure 3. A list of the ACATS
153 instrument parameters is provided in Table 1. The instrument also includes a
154 heating/cooling loop to provide stable thermal operation of the laser.

155 The frequency characteristics of pulsed lasers have recently been advanced due to the
156 development of direct detection Doppler lidars and HSRLs. These techniques impose
157 further requirements compared to standard backscatter lidars, such as lasers that are
158 single frequency on a single pulse basis and more stable in time (central frequency drift
159 of less than 1 MHz per minute). An injection-seeded, pulsed Nd:YAG laser was
160 developed for the TWiLiTE instrument (Hovis *et al.* 2004) that achieves these frequency
161 characteristics. This laser was later replicated for the ACATS instrument and provides a
162 narrow wavelength distribution suitable for resolving the small frequency shifts due to
163 the Doppler effect. The laser operates at an output power of about 10 mJ per pulse and

164 repetition rate of 250 Hz at 532 nm and is designed for use in the low-pressure
165 environment of high-altitude aircraft.

166 The ACATS telescope employs a rotating holographic optic element (HOE) to fit the
167 small volume envelope of the ER-2 superpod and to enable vector wind measurements,
168 which requires more than one viewing direction (Figure 3c). The telescope system is set
169 for 45 degree off-nadir viewing and rotates on a bearing to permit step-stare operation.
170 The number of scan angles (up to 8) and dwell time at each scan angle is controlled by
171 software and can be modified before flight. A schematic of the optical design is presented
172 in Figure 4. As the telescope rotates, the optical alignment changes and may lead to a
173 loss in return signal if not corrected. A procedure that steps the telescope position using
174 piezoelectric actuators and scans for the largest return signal is run during flight to
175 determine the optical alignment at each scan position. The 8-inch diameter telescope is
176 also fiber-coupled to the receiver subsystem to provide greatest flexibility.

177 The primary difference between a lidar system capable of only measuring total
178 backscatter intensity (e.g., CALIOP or CPL) and an instrument that directly measures the
179 particulate extinction and Doppler shift, such as ACATS, lies in the receiver subsystem
180 (Figures 3b; 4). The heart of the ACATS receiver system is an etalon that provides the
181 spectral resolution needed for the HSRL measurement and also to resolve the Doppler
182 shift inherent in the backscattered signal. Backscattered light collected by the telescope
183 is passed through the etalon and an image of the etalon fringe pattern is created. A
184 bandpass filter is used in tandem with the etalon to reject background sunlight, permitting
185 daytime operation. The optical gap of the etalon is 10 cm with an operational diameter of
186 35 mm and plate reflectivity of 85%. As with any MC system, it is critical to maintain

187 the symmetry and shape of the etalon fringe pattern to avoid uncertainty in the
188 measurement. A digital etalon controller was developed by Michigan Aerospace
189 Corporation in which piezoelectric actuators control the etalon electronics to position and
190 maintain the plate parallelism. Considerable work was performed to create autonomous
191 flight software that maintains the etalon alignment over the entirety of an ER-2 flight.
192 The signal transmitted by the etalon is then passed to the detector subsystem.

193 A holographic circle-to-point converter optic (McGill *et al.* 1997c; McGill and
194 Rallison 2001) is placed in the focal plane to provide the spectral detection. The circle-
195 to-point converter simplifies hardware requirements, improves efficiency of measuring
196 the spectral content in the fringe pattern, and allows ACATS to utilize photon-counting
197 detection. The holographic optic is coupled to a Hamamatsu H7260 linear array detector,
198 which utilizes back-end electronics developed by Sigma Space Corporation to permit
199 photon-counting detection at count rates in excess of 50 MHz. The ACATS receiver
200 images ~ 1.2 orders over 24 detector channels. The ACATS etalon parameters result in a
201 measurement dynamic range of ~ 400 m/s, more than sufficient for typical atmospheric
202 motions.

203 An autonomous multi-channel data system is the final component of the instrument
204 and was based entirely on work completed by Sigma Space Corporation in support of the
205 CPL, UAV-CPL, and TWiLiTE lidars. The basis for the data system, the Advanced
206 MultiChannel Scaler (AMCS) card, was first applied in the ER-2 CPL instrument. The
207 data acquisition software is included in the data system and has its heritage in the CPL
208 and UAV-CPL instruments. An important aspect of the ACATS data system, as
209 developed for CPL and UAV-CPL, is the ability to downlink data in real-time from the

210 aircraft using the onboard air and navigation payload server. The data system also
211 incorporates a Novatel model OEMV-3RT2i GPS receiver and OEM-IMU-H58 inertial
212 unit to enable accurate correction for platform motion. The Novatel system provides
213 greater than 20 Hz update rates with 2 cm/s velocity accuracy. The raw ACATS data file
214 consists of photon counts at each horizontal record (1 sec), range bin (30 m) and detector
215 channel, which is then converted to atmospheric parameters such as backscatter and
216 extinction coefficients.

217 ***2.3 ACATS Calibration Procedures***

218 Several calibration parameters are required to accurately retrieve the wind velocity,
219 aerosol and molecular backscatter from the ACATS data. These include normalization
220 constants, instrument defect function parameter, and detector nonlinearity. The
221 illumination and sensitivity of each detector channel are not the same, necessitating
222 normalization constants to compensate. The detector normalization coefficients are
223 determined using a white-light source to illuminate the telescope while the receiving
224 optics remains unchanged. These normalization constants describe the relative response
225 of the detector to broad bandwidth illumination.

226 The alignment of the circle-to-point converter (HOE) and Fabry-Perot fringe pattern
227 also must be characterized. Each ring in the circle-to-point converter represents a
228 detector channel. Since the circle-to-point converter and etalon are manufactured
229 separately, a ring can have a dissimilar centricity and diameter compared to the fringe
230 pattern projected onto it, resulting in signal loss to the corresponding detector channel.
231 To complicate matters, this loss of signal can vary in each channel. In the case of
232 ACATS the outer rings (higher detector channels) of the circle-to-point converter are not

233 perfectly concentric with the fringe pattern, requiring normalization constants to
 234 compensate. The normalization coefficients are determined using the peak transmission
 235 of the etalon calibration data in each channel. Assuming perfect alignment in all
 236 channels, the peak transmission will remain constant as the signal is stepped through all
 237 detector channels. Thus, the ACATS channel with the highest transmission represents
 238 the best alignment, allowing all other channels to be normalized to the “best aligned”
 239 channel. These normalization constants describe the relative signal loss of the detector
 240 channel due to alignment imperfections.

241 To characterize the instrument defect parameter, an etalon calibration procedure has
 242 been developed for ACATS similar to the one outlined in McGill *et al.* (1997a). The
 243 etalon transmission equation as a function of detector channel (j) is expressed as (McGill
 244 1996):

$$245 \quad T(\Delta\lambda, j) = \sum_{n=0}^{\infty} A_n \cos \left[2\pi n \left(\frac{\Delta\lambda}{\Delta\lambda_{FSR}} + \frac{j}{N_{FSR}} \right) \right] \operatorname{sinc} \left(\frac{n}{N_{FSR}} \right) \quad (2.3.1)$$

246 where $\Delta\lambda_{FSR}$ is the free spectral range and is defined as the change in wavelength
 247 necessary to change the order of interference by one. The free spectral range can also be
 248 represented by the number of channels necessary to change the order of interference by
 249 one, N_{FSR} . The function A_n is defined as:

$$250 \quad A_n = 2 \left(1 - \frac{\ell}{1-R} \right)^2 \left(\frac{1-R}{1+R} \right) R^n e^{-4\pi^2 n^2 \Delta d_D^2 \lambda_0^2} \quad (2.3.2)$$

251 where ℓ is the loss of light due to absorption or scattering by the etalon plates and R is
 252 the plate reflectivity. The etalon transmission equation (2.3.1) is for an idealized etalon.

253 A real etalon function will be broadened by several effects, such as plate bowing,
254 microscopic plate defects, detector broadening, and off-axis aberrations.

255 For the purpose of this study, it is sufficient to use an instrument defect parameter
256 (Δd_D) to represent the etalon broadening effects and tune the etalon model so that it
257 matches the measured ACATS spectral response. There are two important assumptions in
258 determining the ACATS defect parameter. First, the defect parameter varies with detector
259 channel to account for the variability of the etalon finesse with channel. It is also assumed
260 that any broadening effects, and thus the etalon defect parameter, will follow a Gaussian
261 distribution. The ACATS defect parameter is then determined by a calibration procedure
262 similar to the one demonstrated in McGill *et al.* (1997a). Software runs a calibration
263 procedure at least once per flight that varies the etalon gap using piezoelectric actuators.
264 Varying the etalon gap moves the interference fringe pattern across the detector in 128
265 small steps, sampling nearly 3 orders (42 points per order). One can then determine the
266 defect parameter for each channel by performing a least-squares fit to match the modeled
267 etalon transmission function to the ACATS measured etalon response function using a
268 similar technique to McGill *et al.* 1997a. The light source used to measure the ACATS
269 etalon response is the same laser that is used for atmospheric measurements.
270 Additionally, the calibration technique automatically compensates for any uncertainty in
271 computing the laser bandwidth, since the laser width follows a Gaussian distribution
272 similar to the etalon broadening term.

273 The measured ACATS spectrum can become distorted due to detector dead time and
274 must be compensated for. All lidar systems that employ photon-counting detection
275 experience this effect, which is a limitation on the number of photons that can be counted

276 in a given time interval. For ACATS, the large near-field return pushes the detector into
277 a nonlinear counting region. The nonlinear effects for this type of detector can be
278 quantified by a detector dead time coefficient. This coefficient represents the fact that
279 only one photon event can be counted at once, and the detector system has a certain time
280 delta, or dead time, before it can count another. A typical Hamamatsu linear array
281 detector, such as the one employed in ACATS, has a discriminator dead time of 65 to 75
282 ns for a discriminator maximum count rate on the order of 15 MHz. To improve this
283 performance, the ACATS Hamamatsu linear array detector is customized with a
284 discriminator built by Sigma Space Corporation under Small Business Innovative
285 Research (SBIR) funding that has a shorter discriminator dead time. This permits
286 photon-counting detection at count rates in excess of 40 MHz before there is a 10%
287 reduction in observed count rate. The ACATS detector rarely experiences count rates
288 higher than 10 MHz in atmospheric bins below 17 km (assuming an ER-2 altitude greater
289 than 19 km). Therefore, the detector dead time coefficient is less than 1.05 for 99.5% of
290 atmospheric bins with the exception of the near-field return.

291 ***3.0 Development of ACATS Retrieval Algorithms***

292 ACATS provides data products similar to other cloud-aerosol lidars, HSRL systems,
293 and Doppler wind lidars. The system is currently set for 45 degree off-nadir viewing and
294 the telescope rotates to allow for two orthogonal line-of-sight (LOS) wind measurements,
295 which are then used to compute vertical profiles of horizontal wind velocity and direction
296 within particulate layers. The ACATS retrieval algorithms and data products for the
297 horizontal wind velocity will be presented at a later date. This paper focuses on two
298 types of aerosol/cloud products available from ACATS data that are directly applicable to

299 the ISS CATS instrument. Standard backscatter products are computed similar to CPL
 300 and CALIPSO (McGill *et al.* 2007). HSRL products are produced at coarser resolutions
 301 (450 m vertical and 5 km horizontal), but include direct retrievals of attenuated
 302 particulate backscatter, optical depth, as well as particulate extinction and backscatter
 303 coefficients. These products are similar to those produced by other HSRL systems.

304 **3.1 Development of Standard Backscatter Algorithms**

305 If the measured ACATS photon counts are summed over all channels as to neglect the
 306 spectral information provided by the etalon, vertical profiles of total backscatter can be
 307 retrieved from ACATS data. Similar to a standard backscatter lidar system (i.e.
 308 CALIOP), this total signal is composed of both the particulate scattering and molecular
 309 scattering. The standard lidar equation can be regrouped and solved for the attenuated
 310 total backscatter (ATB or γ), which has units of $\text{km}^{-1} \text{sr}^{-1}$ and is defined as:

$$311 \quad \gamma(\pi, r) = [\beta_M(\pi, r) + \beta_P(\pi, r)] * e^{-2 \int_0^r \sigma(r') dr} \quad (3.1.1)$$

312 The molecular backscatter coefficient (β_M) is determined from Rayleigh scattering theory
 313 (Tenti *et al.* 1974; Young 1981) and is proportional to atmospheric density. Furthermore,
 314 the molecular extinction coefficient (σ_M) is resolved from the molecular backscatter
 315 coefficient through the relationship $\sigma_M(r) = \beta_M(\pi, r) * (8/3)\pi$. The ACATS standard
 316 ATB is computed using the standard lidar equation and calibrated by normalizing the
 317 signal to the molecular backscatter profile at high altitudes where aerosol loading is
 318 weakest (Russell *et al.* 1979; Del Guasta 1998). This calibration technique is the well-
 319 accepted method of calibrating backscatter lidar signals and is used in CALIPSO and
 320 CPL retrievals (McGill *et al.* 2007). ACATS cloud and aerosol layer boundaries are

321 determined using a similar method to CPL (Yorks *et al.* 2011b). The advantage of using
 322 this retrieval scheme is that the particulate layer properties can be obtained at higher
 323 resolutions, both vertically and horizontally, than using the HSRL retrieval algorithms.
 324 Therefore, this “standard” lidar method is used to compute ACATS attenuated total
 325 backscatter, as well as cloud and aerosol layer boundaries at a vertical resolution of 40 m
 326 and horizontal resolution of 400 m (2 sec).

327 **3.2 Development of HSRL Algorithms**

328 The ACATS HSRL retrieval algorithms are unique and different compared to the
 329 algorithms of current iodine filter HSRL systems (Hair *et al.* 2008). The inclusion of an
 330 etalon in the ACATS instrument design results in a more complicated ACATS lidar
 331 equation compared to the standard lidar equation and iodine filter HSRL equations. The
 332 etalon transmission function (Equation 2.3.1) is convolved with the standard backscatter
 333 lidar equation to yield the expression for the number of photon counts detected per
 334 channel (j), as derived in McGill 1996:

$$\begin{aligned}
 N(r, j) = & \frac{E_T \lambda}{hc} O_A(r) \frac{A_T}{4\pi r^2} \Delta r Q_E T_O T_F(\lambda) \frac{\eta(j)}{n_C} \\
 & \times \sum_{n=0}^{\infty} A_{n,j} \text{sinc}\left(\frac{n}{N_{FSR}}\right) \exp\left(\frac{-\pi^2 n^2 \Delta\lambda_L^2}{\Delta\lambda_{FSR}^2}\right) [\alpha(r) + \omega(r) \exp\left(\frac{-\pi^2 n^2 \Delta\lambda_M^2}{\Delta\lambda_{FSR}^2}\right)] \\
 & \times \cos\left[2\pi n \left(\frac{\lambda_0 - \lambda_C}{\Delta\lambda_{FSR}} - \frac{2U_{LOS}(r)\lambda_0 \sin\varphi}{c\Delta\lambda_{FSR}} - \frac{j}{N_{FSR}}\right)\right]
 \end{aligned}
 \tag{3.2.1}$$

336 The first term represents the instrument parameters and the definitions of individual
 337 parameters are shown in Table 2. The second term contains the laser broadening ($\Delta\lambda_L$),
 338 molecular broadening ($\Delta\lambda_M$), and the atmospheric physics. The attenuated particulate
 339 backscatter (α) and attenuated molecular backscatter (ω) are expressed as:

340
$$\omega(\pi, r) = \beta_M(\pi, r) * e^{-2 \int_0^r \sigma(r') dr} \quad (3.2.2)$$

341
$$\alpha(\pi, r) = \beta_p(\pi, r) * e^{-2 \int_0^r \sigma(r') dr} \quad (3.2.3)$$

342 The Doppler shift is characterized by the second part of the third term, where U_{LOS} is the
 343 LOS wind velocity in ms^{-1} . The attenuated particulate backscatter, attenuated molecular
 344 backscatter, and LOS wind velocity are the three unknown variables in Equation 3.2.1.
 345 Since there are 24 detector channels, the ACATS system is an over-determined set of
 346 equations. These three unknowns are determined using a method developed by McGill *et*
 347 *al.* (1997b). First, the ACATS lidar equation (Equation 3.2.1) is linearized by expanding
 348 the relevant variables in a Taylor series. The equation is then written in matrix form:

349
$$\begin{bmatrix} N_1 - N_{0,1} \\ \cdot \\ \cdot \\ N_{24} - N_{0,24} \end{bmatrix} = \begin{bmatrix} \left. \frac{\partial N_1}{\partial U_{LOS}} \right|_{U_{LOS,0}} & \left. \frac{\partial N_1}{\partial \alpha} \right|_{\alpha_0} & \left. \frac{\partial N_1}{\partial \omega} \right|_{\omega_0} \\ \cdot & \cdot & \cdot \\ \cdot & \cdot & \cdot \\ \left. \frac{\partial N_{24}}{\partial U_{LOS}} \right|_{U_{LOS,0}} & \left. \frac{\partial N_{24}}{\partial \alpha} \right|_{\alpha_0} & \left. \frac{\partial N_{24}}{\partial \omega} \right|_{\omega_0} \end{bmatrix} \begin{bmatrix} U_{LOS} - U_{LOS,0} \\ \alpha - \alpha_0 \\ \omega - \omega_0 \end{bmatrix} \quad (3.2.4)$$

350 This equation can also be written as:

351
$$\Delta N = G \Delta x \quad (3.2.5)$$

352 An iterative weighted least-squares fitting technique is employed to resolve these three
 353 parameters and their corresponding uncertainty, in which the solution is:

354
$$\Delta x^{est} = (G^T W G)^{-1} G^T W \Delta N \quad (3.2.6)$$

355 where W is the weighting matrix and G is the generalized matrix to be inverted. The
 356 solution for the molecular and particulate signals are linear, but non-linear for the
 357 Doppler shift. This least-squares fit method was tested and proven by McGill *et al.*
 358 (1997b) to retrieve the horizontal wind velocity. This work advances the effort of McGill
 359 *et al.* (1997a) and McGill *et al.* (1997b) by developing HSRL retrievals of cloud and
 360 aerosol properties. The first step is to compute the molecular backscatter coefficient (β_M)
 361 and two-way transmission (T_M^2) from Rayleigh scattering theory and meteorological data
 362 from a nearby radiosonde. The definition for the attenuated molecular backscatter (Eq.
 363 3.2.2) can be rewritten in terms of the two-way transmission, corrected for the slant path,
 364 and solved for the two-way particulate transmission (T_p^2):

$$365 \quad T_p^2(r) = \left[\frac{\omega(\pi, r)}{\beta_M(\pi, r) T_M^2(r)} \right]^{\cos\theta} \quad (3.2.7)$$

366 Therefore, the two-way particulate transmission can be determined without making
 367 unnecessary assumptions about the lidar ratio, as in the Klett or Fernald method (Fernald
 368 *et al.* 1972; Klett 1981, 1985). Once T_p^2 is known, the definition of the attenuated
 369 particulate backscatter (Eq. 3.2.3) can be rewritten and used to directly retrieve the
 370 particulate backscatter coefficient (β_p):

$$371 \quad \beta_p(\pi, r) = \frac{\alpha(\pi, r)}{T_M^2(r) T_p^2(r)} \quad (3.2.8)$$

372 The particulate optical depth is then:

$$373 \quad \tau_p(r) = -\frac{1}{2} \ln[T_p^2(r)] \quad (3.2.9)$$

374 The particulate extinction coefficient (σ_p) is directly retrieved using the equation:

375
$$\sigma_p(r) = \frac{\partial \tau_p(r)}{\partial r} \tag{3.2.10}$$

376 and the particulate lidar ratio is:

377
$$S_p(r) = \frac{\sigma_p(r)}{\beta_p(r)} \tag{3.2.11}$$

378 This method is used to compute profiles and layer-integrated values of the
379 aforementioned variables at a vertical resolution of 450 m and horizontal resolution of 5
380 km (25 sec). Their corresponding uncertainties are computed using propagation of errors.
381 If high-resolution optical properties are desired, the directly retrieved lidar ratio can be
382 utilized as a parameterization to compute high-resolution optical properties using the
383 Klett or Fernald method.

384 **4.0 Initial Results from WAVE Campaign**

385 During the period of 9 to 27 September 2012, ER-2 aircraft flights were
386 conducted out of Wallops Island, VA as part of the WAVE project. These flights were
387 planned over land, targeting specific land and vegetation surfaces with a scientific
388 objective of simulating Ice, Cloud and land Elevation Satellite 2 (ICESat-2) data using
389 the Multiple Altimeter Beam Experimental Lidar (MABEL; McGill *et al.* 2013). ACATS
390 was a payload on a total of 13 ER-2 flights, which included observations of thin cirrus
391 clouds, and smoke layers. During these flights, software directed the ACATS telescope to
392 rotate counter-clockwise to four look angle positions denoted by azimuth angle relative to
393 the aircraft nose: 0° (fore), 90° (right), 180° (aft), and 270° (left). At each look angle, the
394 dwell time was set for 60 seconds. The WAVE campaign represents the first science
395 flights for the ACATS instrument in which the telescope rotated and more than one look
396 angle was used. Due to limited time before the project, the telescope alignment was

397 optimized only at the 270-degree look angle. The telescope alignment for the other three
398 look angles was performed in the field using the new and untested in-flight telescope
399 alignment procedure. Portions of flights, and in some cases entire flights, were used to
400 test and refine the etalon calibration procedure and telescope alignment. Furthermore,
401 only two look angles were used for some flights if proper telescope alignment was not
402 achieved at all four look angles. An example of the photon counts summed across all 24
403 detector channels at each of the four look angles from the 26 September 2012 flight is
404 shown in Figure 5 and demonstrates the ability of ACATS to observe cirrus clouds
405 (between 10 and 12 km) at multiple look angles. Overall, ACATS collected science data
406 with high signal-to-noise ratio (SNR) in at least one look angle during 8 of the 13 total
407 flights. The telescope alignment and LOS wind retrievals will be improved before future
408 ACATS flights. This study will focus on ACATS retrievals of cloud and aerosol
409 properties from the WAVE project, particularly those at the 270-degree look angle and
410 high quality data from the other look angles.

411 There were several flights during WAVE in which ACATS collected quality data
412 at multiple look angles. Perhaps the best ACATS performance was on the 26 September
413 ferry flight back to Palmdale, CA when all four look angles were well aligned. Figure 6
414 shows the 532 nm ATB ($\text{km}^{-1} \text{sr}^{-1}$) computed using the standard method (a), the
415 Attenuated Particulate Backscatter ($\text{km}^{-1} \text{sr}^{-1}$) using the HSRL method (b), and the
416 directly-retrieved Particulate Extinction Coefficient (km^{-1}) at the 0 degree look angle (c)
417 for the flight on 26 September 2012. Clearly visible in these images are cloud layers
418 observed by ACATS as the ER-2 flew over the Ohio River Valley (20:28:05 to 21:30:00
419 UTC) and over North Dakota (about 00:24:10 UTC). ACATS also measured a large

420 smoke plume (00:24:10 to 02:10:00 UTC) that extended as high as 6 km over Montana.
421 The images in Figure 6 demonstrate the typical ACATS cloud and aerosol data products.
422 The extinction and backscatter values are typical for cloud and smoke layers and appear
423 to be similar across retrieval methods.

424 The ACATS telescope alignment on the 14 Sep. flight at the 270 degree look
425 angle was the best for the entire campaign, making it a good case to assess biases in the
426 two retrieval methods. Figure 7 shows the 532 nm ATB computed using the standard
427 method (a) and using the HSRL method (b). The latter is essentially $\alpha + \omega$. Cirrus
428 clouds between 9 and 13 km are observed throughout the flight. Figure 8 shows the
429 mean profiles of 532 nm ATB computed using the standard method (blue) averaged to
430 the resolutions of the HSRL products, as well as the ATB using the HSRL method (red)
431 for the grey shaded box in Figure 7b centered around 22:32:22 UTC. Both ATB profiles
432 follow the modeled molecular profile closely above the cirrus layer and show similar
433 structure inside the cirrus layer. The standard ATB retrieval is about 10 percent higher
434 than the ATB computed using the HSRL method within the cirrus layer. This difference
435 is likely due to the errors in the calibration technique used in both retrievals. The error in
436 the CPL calibration constant is estimated to be around 5 percent at 532 nm due to signal
437 noise and the presence of aerosols in the CPL calibration zone (Campbell *et al.*, 2008;
438 Vaughan *et al.* 2010). Errors in the determination of the etalon defect parameter can lead
439 to errors of as much as 5 percent in the HSRL retrieved attenuated molecular and
440 particulate backscatter. Although this comparison provides confidence in the ACATS
441 HSRL algorithms, it does not resolve any possible instrument biases. To address this

442 issue, the ACATS standard backscatter and HSRL products are compared to coincident
443 CPL cloud and aerosol properties during the WAVE campaign in a companion paper.

444 **5.0 Summary**

445 A new multi-channel direct-detection Doppler wind lidar has been developed at
446 NASA GSFC for use on the NASA ER-2 called the Airborne Cloud-Aerosol Transport
447 System (ACATS). ACATS employs a Fabry-Perot interferometer to provide the spectral
448 resolution needed to retrieve the Doppler shift, similar to the ground-based University of
449 Michigan MC direct-detection Doppler wind lidar (McGill *et al.* 1997a). The ACATS
450 instrument design includes a seeded laser and circle-to-point converter, as well as a
451 heating/cooling loop for stable laser performance during airborne operation. The ACATS
452 telescope rotates to four look angles to permit the retrieval of the horizontal wind velocity
453 within atmospheric layers. ACATS also advances the technology of a MC direct-
454 detection Doppler wind lidar by demonstrating the utility of such an instrument for HSRL
455 retrievals of cloud and aerosol properties.

456 The nature of a MC direct-detection Doppler wind lidar such as ACATS permits
457 three types of cloud and aerosol lidar retrievals: standard backscatter lidar products such
458 as ATB and layer boundaries, directly retrieved cloud and aerosol optical properties such
459 as extinction and lidar ratio using the HSRL technique, and horizontal wind velocity of
460 the cloud or aerosol particles within an atmospheric layer. This paper outlines the
461 retrieval algorithms for all two of these types of ACATS data products, focusing on the
462 HSRL derived cloud and aerosol properties. The first ACATS science flights were
463 conducted during the WAVE project in September 2012. Initial results demonstrate the
464 effectiveness of ACATS as an airborne HSRL system. The HSRL ATB retrieval for

465 cirrus observed during the 14 September flight at the 270-degree look angle agrees with
466 the ATB derived using the standard backscatter method to within 10 percent. Since the
467 ISS CATS HSRL receiver is designed similar to ACATS, the algorithms and data
468 products developed for ACATS have direct application to this future spaceborne mission
469 Furthermore, the ACATS HSRL and wind products can be used for science applications
470 such as aerosol transport, smoke plume properties and convective outflow in tropical
471 storms.

472 **Acknowledgments**

473 NASA's Earth Science Technology Office (ESTO) Advanced Component
474 Technology (ACT) program funded the development of the ACATS receiver subsystem.
475 NASA's Airborne Instrument Technology Transfer (AITT) program funded ACATS
476 instrument integration and ER-2 test flights. A special thanks to all the engineers at
477 Sigma Space Corporation that were involved in building ACATS. We also thank Russ
478 Dickerson for valuable discussions.

479 **References**

- 480 Abreu, V. J., J. E. Barnes, and P. B. Hays, 1992: Observations of winds with an
481 incoherent lidar detector, *Appl. Opt.*, **31**, 4509–4514.
- 482 Ackermann J., 1998: The extinction-to-backscatter ratio of tropospheric aerosol:
483 numerical study. *J. Atmos. Oceanic Technol.*, **15**, 1043–1050.
- 484 Baker, W, and Coauthors, 1995: Lidar-measured winds from space: a key component for
485 weather and climate prediction. *BAMS*, **76**, 869-888
- 486 Benedetti-Michelangeli, G., F. Congeduti, and G. Fiocco, 1972: Measurement of aerosol
487 motion and wind velocity in the lower troposphere by Doppler optical lidar, *J.*
488 *Atmos. Sci.*, **29**, 906–910.
- 489 Chanin, M. L., A. Garnier, A. Hauchecorne, and J. Porteneuve, 1989: A Doppler lidar for
490 measuring winds in the middle atmosphere, *Geophys. Res. Lett.*, **16**, 1273–1276.
- 491 Comstock, J. M., T. P. Ackerman, and G. G. Mace, 2002: Groundbased lidar and radar
492 remote sensing of tropical cirrus clouds at Nauru Island: Cloud statistic and
493 radiative impacts. *J. Geophys. Res.*, **107**, 4714, doi:10.1029/2002JD002203.
- 494 Del Guasta, M., 1998: Errors in the retrieval of thin-cloud optical parameters obtained
495 with a two-boundary algorithm, *Appl. Opt.*, **37**, 5522–5540.

496 Esselborn, M., M. Wirth, A. Fix, M. Tesche, and G. Ehret, 2008: Airborne high spectral
497 resolution lidar for measuring aerosol extinction and backscatter coefficients.
498 *Appl. Opt.*, **47**, 346–358.

499 Fernald, F.G., B. M. Herman and J. A. Reagan, 1972: “Determination of aerosol height
500 distributions with lidar”, *Journal of Applied Meteorology*, **11**, 482-489.

501 Fiocco, G., G. Beneditti-Machelangeli, K. Maschberger, and E. Madonna, 1971:
502 *Nature Phys. Sci.*, **229**, 78.

503 Fischer, K. W., V. J. Abreu, W. R. Skinner, J. E. Barnes, M. J. McGill, and T. D. Irgang,
504 1995: Visible wavelength Doppler lidar for measurement of wind and aerosol
505 profiles during day and night, *Opt. Eng.*, **34**, 499–511.

506 Garnier, A. and M. L. Chanin, 1992: Description of a Doppler Rayleigh LIDAR for
507 measuring winds in the middle atmosphere, *Appl. Phys.*, **55**, 35–40.

508 Gentry, B. and C. L. Korb, 1994: Edge technique for high accuracy Doppler velocimetry,
509 *Appl. Opt.*, **33**, 5770–5777.

510 Grund C. J., and E.W. Eloranta, 1991: University of Wisconsin high spectral resolution
511 lidar. *Opt. Eng.*, **30**, 6–12.

512 Hair, J. W., and Coauthors, 2008: Airborne High Spectral Resolution Lidar for profiling
513 aerosol optical properties. *Appl. Opt.*, **47**, 6734–6752.

514 Hall Jr., F. F., R. M. Huffaker, R. M. Hardesty, M. E. Jackson, T. R. Lawrence, M. J.
515 Post, R. A. Richter, and B. F. Weber, 1984: Wind measurement accuracy of the
516 NOAA pulsed infrared Doppler lidar, *Appl. Opt.*, **23**, 2503–2506.

517 Hovis, F.E. , M. Rhoades, R. L. Burnham, J. D. Force, T. Schum, B. M. Gentry, H. Chen,
518 S. X. Li, J. W. Hair, A. L. Cook, and C. A. Hostetler, 2004: Single-frequency
519 lasers for remote sensing. *Proc. SPIE* 5332, 263–270.

520 Huffaker, R. M., T. R. Lawrence, M. J. Post, J. T. Priestly, F. F. Hall Jr., R. A. Richter,
521 and R. J. Keeler, 1984: Feasibility studies for a global wind measuring satellite
522 system Windsat: analysis of simulated performance, *Appl. Opt.*, **23**, 2532–2536.

523 Jensen, E. J., Lawson, P., Baker, B., Pilson, B., Mo, Q., Heymsfield, A. J., Bansemer, A.,
524 Bui, T. P., McGill, M., Hlavka, D., Heymsfield, G., Platnick, S., Arnold, G. T.,
525 and Tanelli, S., 2009: On the importance of small ice crystals in tropical anvil
526 cirrus, *Atmos. Chem. Phys.*, **9**, 5519-5537, doi:10.5194/acp-9-5519-2009.

527 Klett, J. D., 1981: Stable analytical inversion solution for processing lidar returns. *Appl.*
528 *Opt.*, **20**, 211–220.

529 Klett, J. D., 1985: Lidar inversion with variable backscatter/extinction ratios. *Appl. Opt.*,
530 **24**, 1638–1643.

531 Lee, W.C., P. Dodge, F.D. Marks, P.H. Hildebrand, 1994: Mapping of airborne Doppler
532 radar data, *J. Atmos. Oceanic Technol.*, **11**, 572–578.

533 Leon, D., and G. Vali, 1998: Retrieval of Three-Dimensional Particle Velocity from
534 Airborne Doppler Radar Data, *J. Atmos. Oceanic Technol.*, **15**, 860–870.

535 McGill, M.J., 1996: Recovery and Validation of Wind and Aerosol Profiles from
536 Incoherent Doppler Lidar Measurements. PhD Thesis, University of Michigan
537 (Ann Arbor, MI).

538 McGill, M. J., W. R. Skinner, and T. D. Irgang, 1997a: Analysis techniques for the
539 recovery of winds and backscatter coefficients from a multiple channel incoherent
540 Doppler lidar, *Appl. Opt.*, **36**, 1253–1268.

541 McGill, M. J., W. R. Skinner, and T. D. Irgang, 1997b: Validation of wind profiles

542 measured using incoherent Doppler lidar, *Appl. Opt.*, **36**, 1928–1939.

543 McGill, M. J., M. Marzouk, V. S. Scott, and J. D. Spinhirne, 1997c: Holographic circle-
544 to-point converter with particular applications for lidar work, *Opt. Eng.*, **36**,
545 2171–2175.

546 McGill, M.J., and J.D. Spinhirne, 1998: Comparison of two direct-detection Doppler lidar
547 techniques, *Opt. Eng.*, **37**, 2675–2686.

548 McGill, M.J., and R.D. Rallison, 2001: Holographic optics convert rings to points for
549 Detection. *Laser Focus World*, **37**, 131-136.

550 McGill, M. J., D. Hlavka, W. Hart, V. S. Scott, J. Spinhirne, and B. Schmid, 2002: Cloud
551 Physics Lidar: instrument description and initial measurement results. *Applied*
552 *Optics*, **41**, 3725-3734.

553 McGill, M. J., M. A. Vaughan, C. R. Trepte, W. D. Hart, D. L. Hlavka, D. M. Winker,
554 and R. Kuehn, 2007: Airborne validation of spatial properties measured by the
555 CALIPSO lidar. *J. Geophys. Res.*, **112**, D20201, doi:10.1029/2007JD008768.

556 McGill, Matthew, Thorsten Markus, V. Stanley Scott, Thomas Neumann, 2013: The
557 Multiple Altimeter Beam Experimental Lidar (MABEL): An Airborne Simulator
558 for the ICESat-2 Mission. *J. Atmos. Oceanic Technol.*, **30**, 345–352.
559 doi: <http://dx.doi.org/10.1175/JTECH-D-12-00076.1>

560 Piironen P. and E.W. Eloranta, 1994: Demonstration of a high-spectral-resolution lidar
561 based on an iodine absorption filter. *Opt. Lett.*, **19**, 234–236.

562 Russell, P. B., T. J. Swissler, and M. P. McCormick, 1979: Methodology for error
563 analysis and simulation of lidar aerosol measurements, *Appl. Opt.*, **18**, 3783–
564 3797.

565 Schwiesow, R.L., F. Köpp, and C. Werner, 1985: Comparison of Lidar-Measured Wind
566 Values Obtained by Full Conical Scan, Conical Sector Scan, and Two Point
567 Techniques, *J. Atmos. Oceanic Technol.*, **2**, 3.

568 Shipley, S. T., D. H. Tracy, E. W. Eloranta, J. T. Tauger, J. T. Sroga, F. L. Roesler, and J.
569 A. Weinman, 1983: High spectral resolution lidar to measure optical scattering
570 properties of atmospheric aerosols. 1: Theory and instrumentation. *Appl. Opt.*, **22**,
571 3716–3724.

572 Spinhirne, J. D., S. P. Palm, W. D. Hart, D. L. Hlavka, and E. J. Welton, 2005: Cloud and
573 aerosol measurements from GLAS: Overview and initial results. *Geophys. Res.*
574 *Lett.*, **32**, L22S03, doi:10.1029/2005GL023507.

575 Tenti, G., C. D. Boley, and R. C. Desai, 1974: On the kinetic model description of
576 Rayleigh–Brillouin scattering from molecular gases. *Can. J. Phys.*, **52**, 285–290.

577 Vaughan, M.A., Z. Liu, M.J. McGill, and M.D. Obland, 2010: On the spectral
578 dependence of backscatter from cirrus clouds: an assessment of CALIOP’s 1064
579 nm calibration using Cloud Physics Lidar measurements, *Atmospheric Chemistry*
580 *and Physics*.

581 Werner, C., 2005: “Doppler Wind Lidar,” in *Lidar: Range-Resolved Optical Remote*
582 *Sensing of the Atmosphere*, C. Weitkamp, ed. (Springer), 325-354.

583 Whiteman, D. N., B. Demoz, and Z. Wang, 2004: Subtropical cirrus cloud extinction to
584 backscatter ratios measured by Raman Lidar during CAMEX-3. *Geophys. Res.*
585 *Lett.*, **31**, L12105, doi:10.1029/2004GL020003.

586 Winker, D. M., M. A. Vaughan, A. H. Omar, Y. Hu, K. A. Powell, Z. Liu, W. H. Hunt,

587 and S. A. Young, 2009: Overview of the CALIPSO Mission and CALIOP Data
588 Processing Algorithms. *J. Atmos. Oceanic Technol.*, **26**, 1105-1119,
589 doi:10.1175/2009JTECHA1281.1.

590 Yorks, J. E., D. L. Hlavka, W. D. Hart, M. J. McGill, 2011a: Statistics of Cloud Optical
591 Properties from Airborne Lidar Measurements. *J. Atmos. Oceanic Technol.*, **28**,
592 869–883. doi: <http://dx.doi.org/10.1175/2011JTECHA1507.1>

593 Yorks, J. E., D. L. Hlavka, M. A. Vaughan, M. J. McGill, W. D. Hart, S. Rodier, and R.
594 Kuehn, 2011b: Airborne validation of cirrus cloud properties derived from
595 CALIPSO lidar measurements: Spatial properties, *J. Geophys. Res.*, **116**, D19207,
596 doi:10.1029/2011JD015942.

597 Young, A.T., 1981: Rayleigh scattering. *Phys. Today*, **35**, 42–48.

598 Young, S. A., and M. A. Vaughan, 2009: The retrieval of profiles of particulate
599 extinction from Cloud-Aerosol Lidar Infrared Pathfinder Satellite Observations
600 (CALIPSO) data: Algorithm description. *J. Atmos. Oceanic Technol.*, **26**, 1105–
601 1119.

602 Young, Stuart A., Mark A. Vaughan, Ralph E. Kuehn, David M. Winker, 2013: The
603 Retrieval of Profiles of Particulate Extinction from Cloud–Aerosol Lidar and
604 Infrared Pathfinder Satellite Observations (CALIPSO) Data: Uncertainty and
605 Error Sensitivity Analyses. *J. Atmos. Oceanic Technol.*, **30**, 395–428.
606 doi: <http://dx.doi.org/10.1175/JTECH-D-12-00046.1>

607 Zhao, Y., G. G. Mace, and J. M. Comstock, 2011: The occurrence of particle size
608 distribution bimodality in midlatitude cirrus as inferred from ground-based remote
609 sensing data, *J. Atmos. Sci.*, **68**, 1162–1177, doi:10.1175/2010JAS3354.1.

610
611
612
613 **Table 1.** Primary system parameters for ACATS lidar.

Parameter	Value
Laser Type	Nd: YAG, seeded
Wavelength	532 nm
Laser Repetition Rate	250 Hz
Laser Output Energy	~10 mJ/pulse
Telescope Diameter	8 inches
Viewing Angle	45 degrees
Telescope FOV	350 μ radians (full angle)
Bandpass Filter	150 pm FWHH
Etalon Spacing	10 cm
Etalon Reflectivity	85%
Orders Imaged	1.2
Detector Channels	24
Raw Range Resolution	30 m
Horizontal Resolution	1 sec (~200 m)
Platform Speed	~200 m/s
Platform Altitude	~ 20 km (65,000 ft)

614

615
616
617
618
619
620
621
622

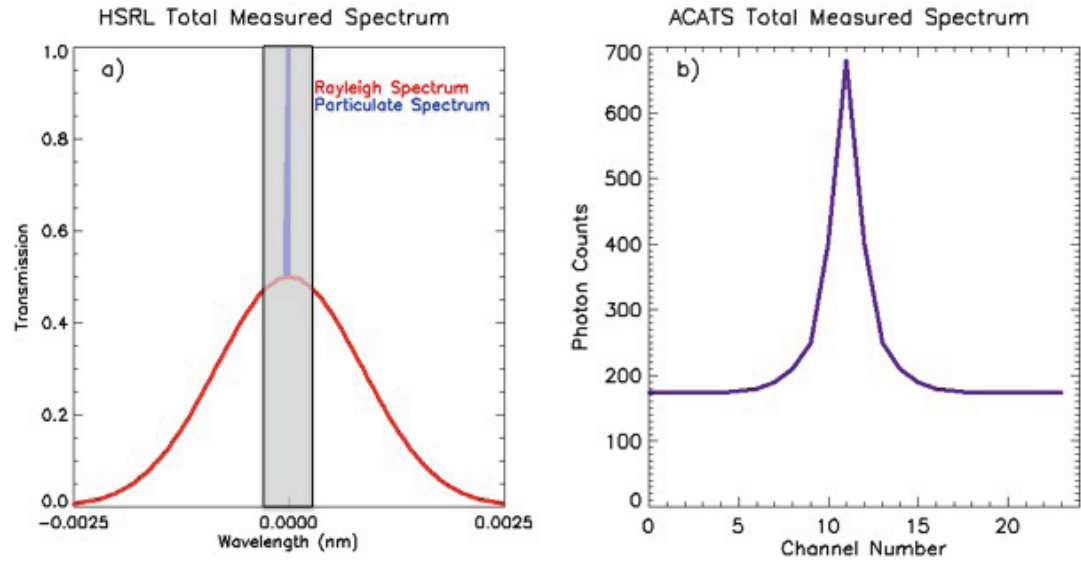
Table 2. Definitions of parameters found in the ACATS lidar equation

Variable	Definition	Units
$N(r)$	number of photons detected per range bin	-
r	distance to the scattering particle	m
j	detector channel	-
E_T	transmitted laser energy	J
λ	laser wavelength	m
h	Planck's constant	J sec
c	speed of light	$m\ s^{-1}$
A_T	area of lidar telescope	m^2
Δr	range bin width	m
Q_E	detector quantum efficiency	-
T_O	system optical efficiency	-
T_F	optical filter efficiency	-
$O_A(r)$	overlap function	-
n_c	number of detector channels	-
η_c	detector normalization	-
N_{FSR}	free spectral range (channel number)	-
$\Delta\lambda_{FSR}$	free spectral range (wavelength)	m^{-1}
$\Delta\lambda_L$	laser broadening 1/e width (wavelength)	m^{-1}
$\Delta\lambda_M$	molecular broadening 1/e width (wavelength)	m^{-1}
$\alpha(r)$	attenuated particulate backscatter coefficient	$m^{-1}\ sr^{-1}$
$\omega(r)$	attenuated molecular backscatter coefficient	$m^{-1}\ sr^{-1}$
φ	off-nadir pointing angle	degrees
U_{LOS}	LOS wind velocity	$m\ s^{-1}$
λ_c	center position of the laser linewidth	m
λ_c	center wavelength of the etalon	m

623
624
625
626
627
628
629
630
631
632

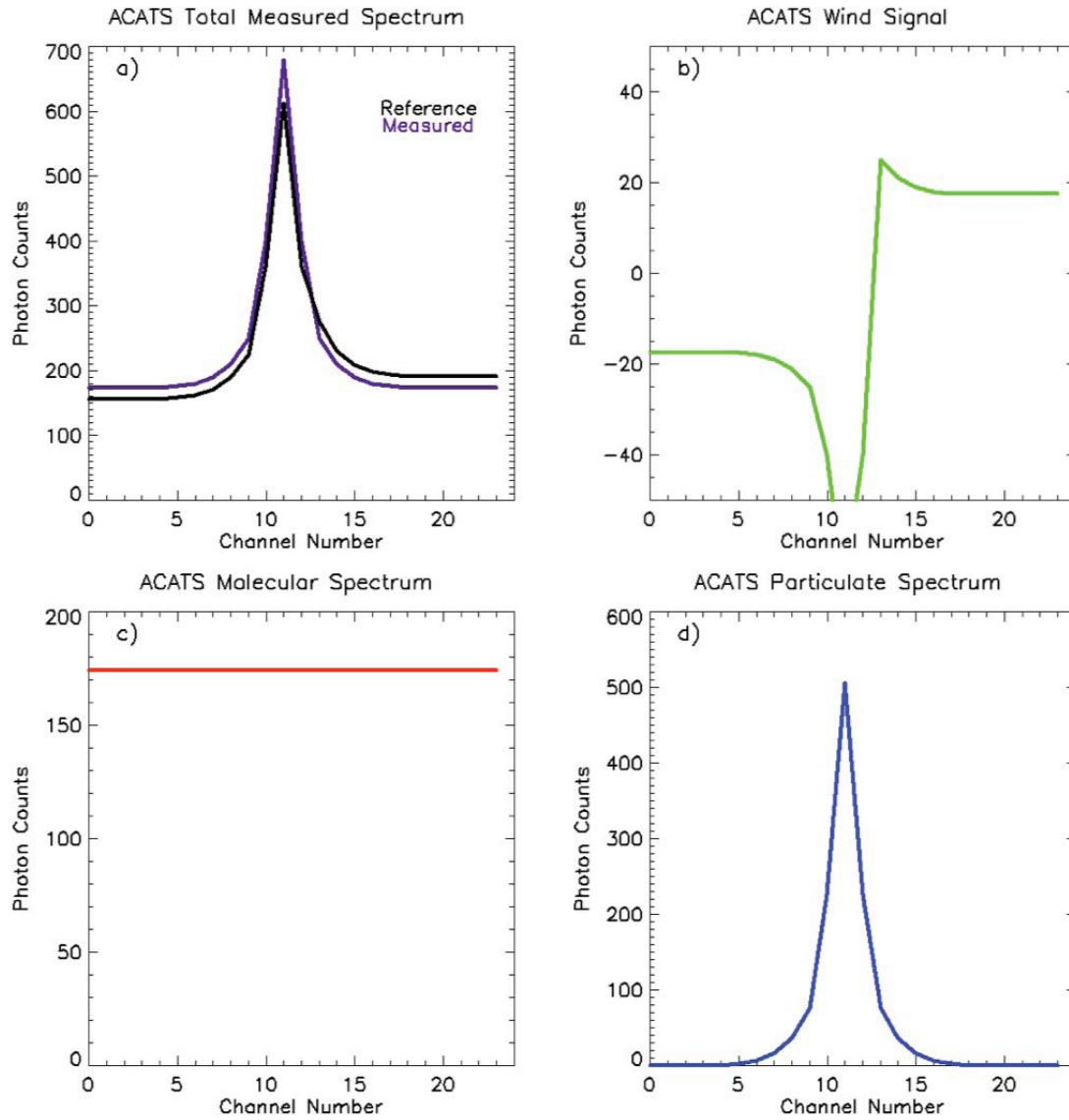
633
634
635
636
637
638
639
640

Figures



641
642
643
644
645

Figure 1. The ACATS method images the grey shaded area of the returned atmospheric signal (a) onto a 24 channel array detector, which measures the photon counts at each wavelength interval independently as a total backscattered signal (b).



646
647
648
649
650
651

Figure 2. The Doppler shifted atmospheric signal (purple) measured by ACATS is compared to an unshifted reference spectrum (a), which yields the Doppler wind signal (b) of the ACATS measurement. The broad Rayleigh scattered spectrum (c) is measured by ACATS as a nearly flat background of the total atmospheric return signal, resulting in a sharp particulate spectrum (d) that is directly measured.



652

653

654

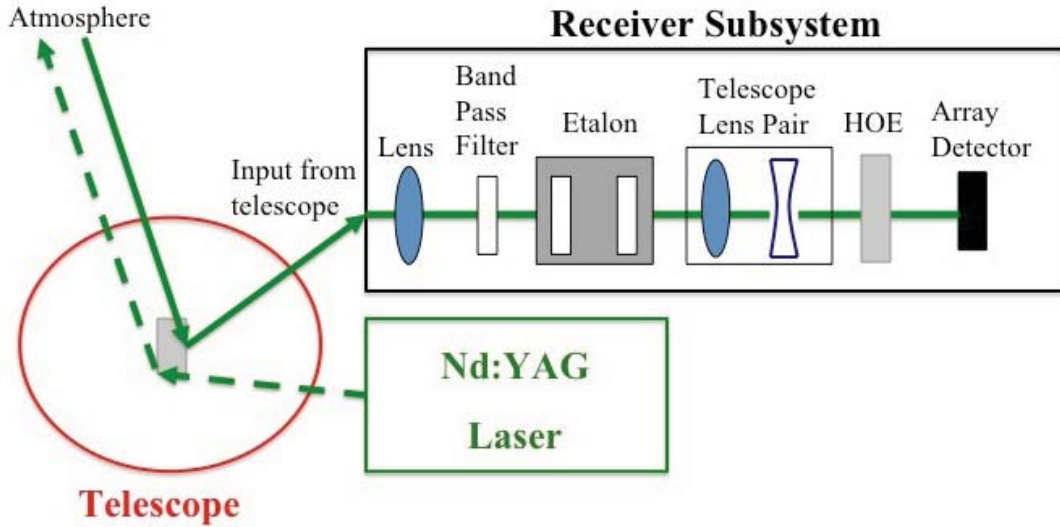
655

656

657

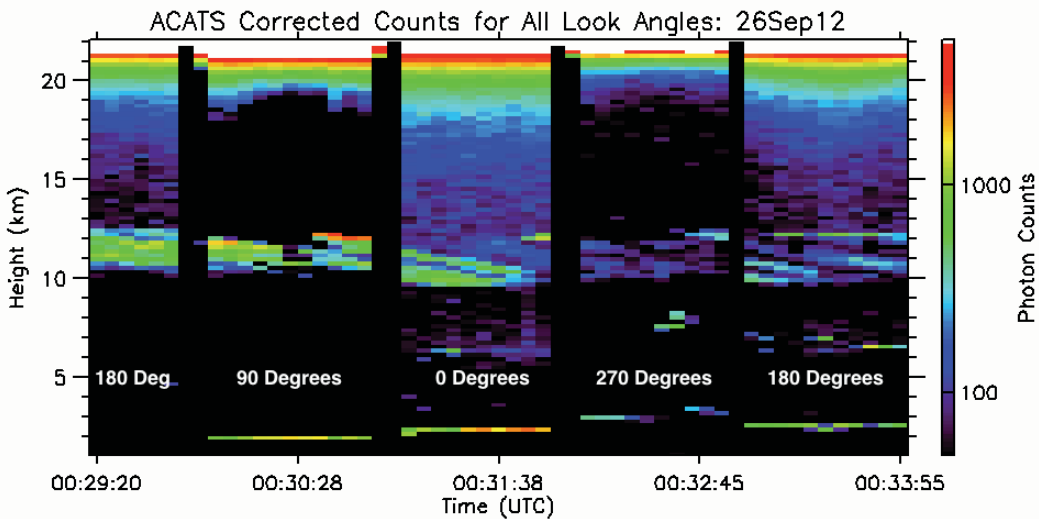
Figure 3. The fully assembled ACATS instrument (a) includes the receiver tube covered in insulation (left) and a pressurized telescope dome (right). A picture of the inside of the receiver subsystem (b) shows the etalon (silver device in the middle), the 24-channel array detector, and circle-to-point converter. The inside of the telescope subsystem (c) contains a motor to rotate the telescope and a HOE.

ACATS Optical Schematic



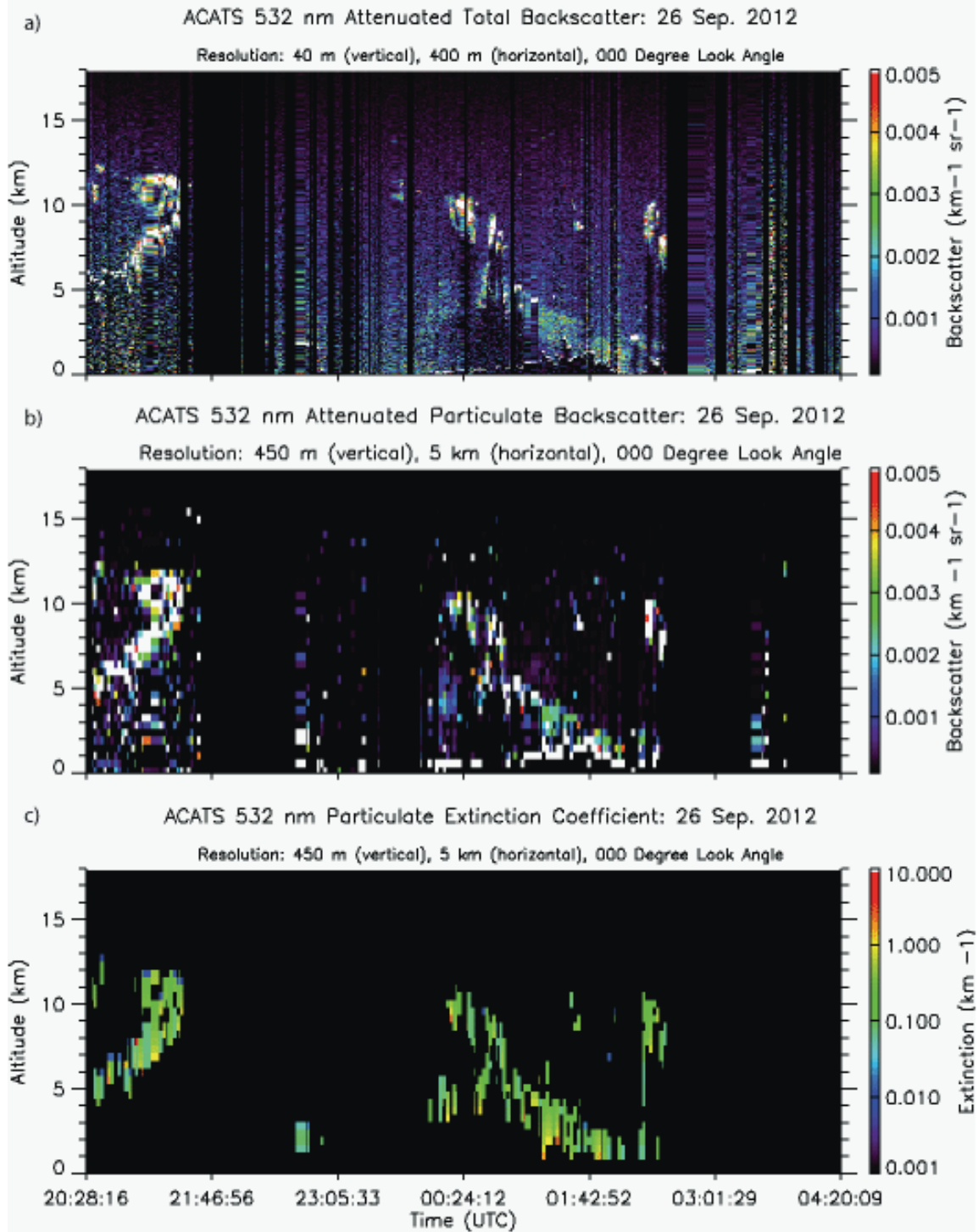
658
659
660
661
662
663

Figure 4. The ACATS optical schematic shows the outgoing 532 nm laser light (dashed green), originating from the Nd:YAG laser, directed out of the telescope by a mirror. The return signal (solid green) is passed through the telescope and into the receiver subsystem using an optical fiber, where it is transmitted through optical lenses and filters, including the etalon.



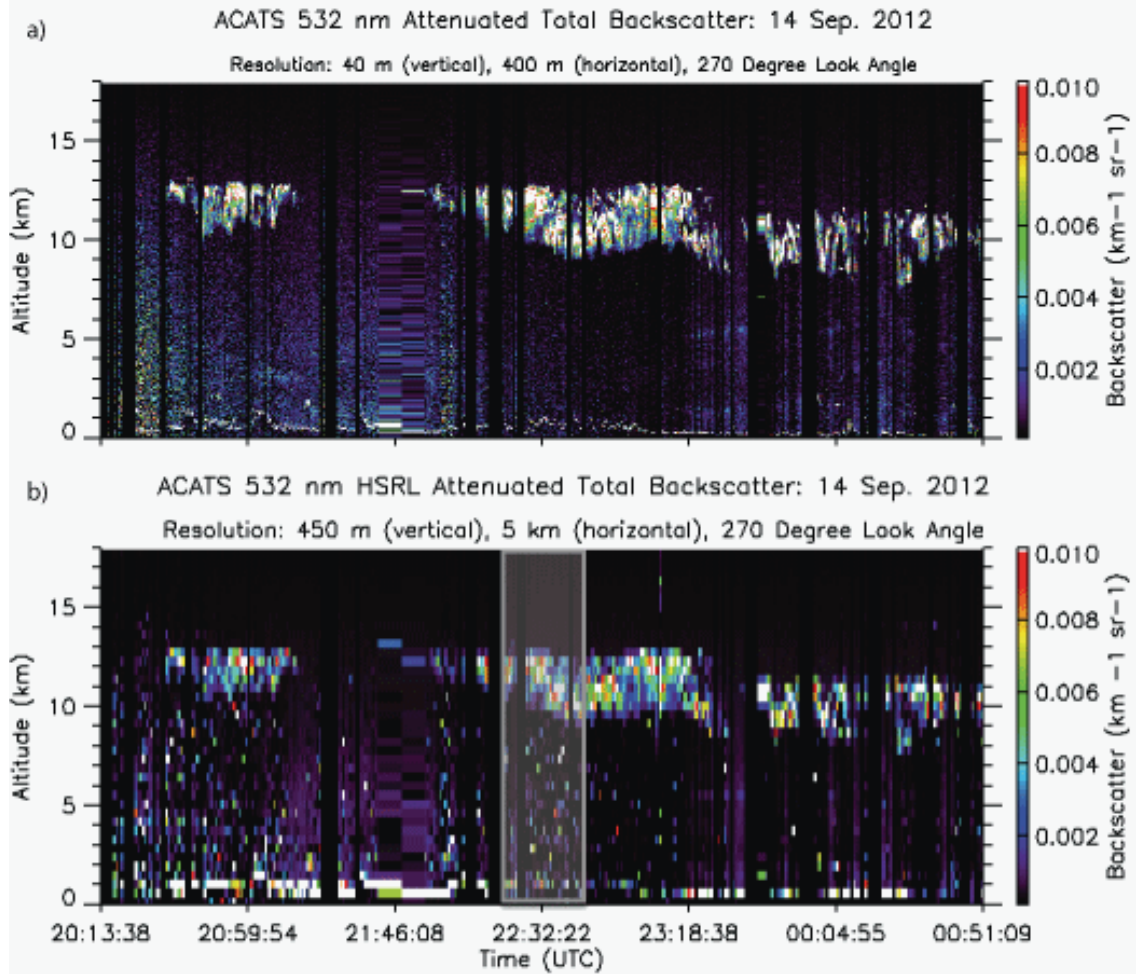
664
665
666
667

Figure 5. ACATS photon counts from an ER-2 flight on 26 September 2012. The high count rates between 10 and 12 km show the detection of a cirrus layer at all four look angles at intervals of 60 seconds.



668
669
670
671
672
673
674

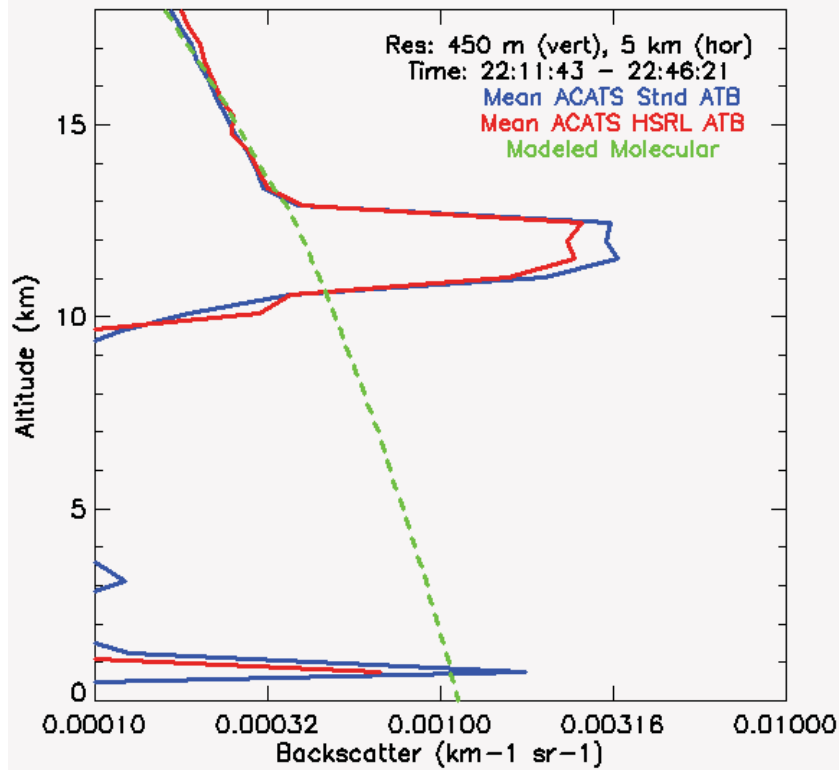
Figure 6. The ACATS 532 nm Attenuated Total Backscatter ($\text{km}^{-1} \text{sr}^{-1}$) computed using the standard method (a), the Attenuated Particulate Backscatter ($\text{km}^{-1} \text{sr}^{-1}$) derived using the HSRL method (b), and the directly-retrieved Particulate Extinction Coefficient (km^{-1}) at the 0 degree look angle (c) for the ER-2 flight on 26 September. ACATS observed clouds as the ER-2 flew over the Ohio River Valley (20:28:05 to 21:30:00 UTC) and a large smoke plume (00:24:10 to 02:10:00 UTC) that extended as high as 6 km over Montana.



675
676
677
678
679

Figure 7. The ACATS 532 nm Attenuated Total Backscatter computed using the standard method (a) and using the HSRL method (b) at the 270 degree look angle for the ER-2 flight on 14 September. The grey box focuses on a 35 minute segment in which the mean profiles are compared in Figure 8 for cirrus clouds.

ACATS Backscatter (270 deg): 14 Sep. 2012



680
681
682
683
684

Figure 8. The ACATS mean profiles of 532 nm Attenuated Total Backscatter computed using the standard method (blue) averaged to the resolutions of the HSRL products, as well as the Attenuated Total Backscatter using the HSRL method (red) for the grey shaded box in Figure 7b (22:11:43 – 22:46:21 UTC).